Research Square

Preprints are preliminary reports that have not undergone peer review.
They should not be considered conclusive, used to inform clinical practice,
or referenced by the media as validated information.

Radio continuum emission in the edge-on galaxy NGC~5729

Camila Ailen Galante

cgalante@iar.unlp.edu.ar

Instituto Argentino de Radioastronomía

Juliana Saponara

Instituto Argentino de Radioastronomía

Gustavo Esteban Romero

Instituto Argentino de Radioastronomía

Paula Benaglia

Instituto Argentino de Radioastronomía

Research Article

Keywords: Radio continuum emission, Radio sources, Individual galaxies, Spiral galaxies

Posted Date: November 12th, 2026

DOI: https://doi.org/10.21203/rs.3.rs-11516151/v1

License: This work is licensed under a Creative Commons Attribution 4.0 International License.
Read Full License

Additional Declarations: No competing interests reported.

Radio continuum emission in the edge-on galaxy NGC 5729

C. A. Galante[1,2*], J. Saponara[1,2], G. E. Romero[1,2], P. Benaglia[1]

[1]Instituto Argentino de Radioastronomía (CONICET–CIC–UNLP), C.C. No. 5, 1894, Villa Elisa, Buenos Aires, Argentina.

[2]Facultad de Ciencias Astronómicas y Geofísicas, Universidad Nacional de La Plata (UNLP), Paseo del Bosque s/n, B1900FWA, La Plata, Buenos Aires, Argentina.

*Corresponding author(s). E-mail(s): cgalante@iar.unlp.edu.ar;

Abstract

We present Jansky Very Large Array observations at 1.5 and 3 GHz of the edge-on spiral galaxy NGC 5729 to investigate its vertical radio structure and discrete source population. Fits to the vertical intensity profiles yield radio scale heights lower than 1 kpc, showing that the non-thermal emission is vertically compact. Despite a star formation rate surface density above empirical thresholds for radio halo formation, NGC 5729 lacks an extended extraplanar halo. The scale height ratio of 1.88 ± 0.07 indicates a strong frequency dependence, consistent with advective transport at low velocities dominated by synchrotron cooling. We also report three compact radio sources, highlighted by NGC 5729-R1 in the northern disk, which is the brightest radio feature in the galaxy. NGC 5729-R1 remains unresolved ($\lesssim 200 - 250$ pc), displaying a steep spectral index ($\alpha = -0.9 \pm 0.1$) and a 1.5 GHz spectral luminosity of 1.4×10^{27} erg s^{-1} Hz^{-1}, consistent with a powerful microquasar nebula or a ULX-driven bubble. Secondary sources R2 and R3 exhibit non-thermal spectra consistent with supernova remnants or compact remnant complexes.

Keywords: Radio continuum emission, Radio sources, Individual galaxies, Spiral galaxies

1 Introduction

Edge-on galaxies provide ideal laboratories for distinguishing the thin and thick disks and, therefore, studying the disk-halo interface. The thin disk is composed of stars, dust, neutral and molecular gas, while the thick disk contains warm ionized gas, cosmic rays (CRs), and a large-scale magnetic field (Ferrière 2001; Cox 2005). In the literature, the thick disk is commonly referred to as the extraplanar component. Consequently, this region links the star-forming midplane with the circumgalactic medium (CGM), a major baryon reservoir (Tumlinson et al. 2017), which makes it a natural place to trace outflows, fountains, and accretion. In the radio continuum, many edge-on spirals display prominent synchrotron halos extending several kiloparsecs above the disk plane (e.g. Wiegert et al. 2015; Krause et al. 2018; Heesen et al. 2025; Galante et al. 2024). This emission arises from relativistic cosmic-ray electrons (CRe) gyrating in galactic magnetic fields (e.g. Vargas et al. 2019).

Because cosmic-ray electrons are ultimately linked to massive-star formation and supernova activity, the radio continuum luminosity is closely connected to stellar feedback across galactic disks. As a result, the global correlation between radio continuum emission and star formation rate (SFR) is well established, with a near-linear slope at gigahertz frequencies (Li et al. 2016). On resolved,

kiloparsec scales, however, the local relation becomes sub-linear because cosmic-ray transport diffuses relativistic electrons away from their injection sites in star-forming regions into quiescent areas (Heesen et al. 2023). When examined as a function of height above the galactic plane, this relation shows distinct regimes: the thin disk exhibits a near- or super-linear relation dominated by newly injected cosmic-ray electrons, and the thick disk and halo exhibit a sub-linear relation shaped by cosmic-ray diffusion and spectral aging (e.g. Heesen et al. 2025). Investigating galaxies in which the radio emission has a relatively low scale height is therefore crucial for testing the limits of cosmic-ray propagation and the conditions under which an extended thick radio component does not develop.

While substantial progress has been made in characterizing galaxies with prominent halos associated with starbursts or galactic winds (e.g. Mora-Partiarroyo et al. 2019; Heald et al. 2022), systems with vertically compact radio emission remain comparatively less explored. Galaxies with low star formation rate surface densities ($\Sigma_{\rm SFR}$) and deep gravitational potentials offer a critical benchmark to establish the threshold conditions required to transport cosmic rays and magnetic fields into the circumgalactic medium (e.g. Schmidt et al. 2019; Xu et al. 2026). In such quiescent systems, extraplanar radio emission, when present, can remain weak and vertically compact, with scale heights substantially smaller than those observed in galaxies hosting extended radio halos. The vertical profiles of this emission can be approximately Gaussian, consistent with diffusive cosmic-ray transport, in which cosmic-ray electrons gradually lose energy as they propagate away from the star-forming disk.

NGC 5729 is a highly inclined ($i \sim 83.8°$) spiral galaxy classified as Sb pec, located at a distance of 19.7 Mpc (Wang and Rowan-Robinson 2009). The galaxy is part of a small, loose group comprising three members (Giuricin et al. 2000). Its infrared luminosity derived from IRAS data is $\log(L_{\rm IR}/{\rm L}_\odot) = 10.04$, corresponding to an estimated star formation rate of 1.6 $\mathrm{M}_\odot\,\mathrm{yr}^{-1}$. An independent estimate based on the WISE infrared luminosity reported by Cluver et al. (2025) yields a lower star formation rate of 0.9 $\mathrm{M}_\odot\,\mathrm{yr}^{-1}$. The same study estimates a stellar mass of 6.5×10^9 $\mathrm{M}_\odot$ for NGC 5729. Radio and infrared diagnostics indicate that its global emission is consistent with being dominated by processes associated with recent star formation rather than by an active nucleus (Condon et al. 2019).

Previous radio continuum information for NGC 5729 is limited to the NRAO VLA Sky Survey (NVSS Condon et al. 1998), with a reported total flux density of 47 ± 2 mJy at 1.4 GHz. However, the angular resolution of the NVSS is insufficient to investigate the vertical radio structure of NGC 5729 in detail. To our knowledge, no previous study has used spatially resolved, multi-frequency radio observations to characterize the extraplanar emission of NGC 5729. Its high inclination and ongoing star formation therefore make it a useful target for investigating its radio continuum morphology and vertical structure. The main properties of NGC 5729 are listed in Table 1.

Table 1 Main properties of NGC 5729.

Parameter	Value	Reference
$\mathrm{RA_{J2000}}$	$14^{\rm h}42^{\rm m}06^{\rm s}$	(1)
$\mathrm{DEC_{J2000}}$	$-09°00'34''$	(1)
Morph. type	Sb pec	(1)
Distance [Mpc]	19.7	(2)
Inclination [°]	83.8	(3)
Pos. angle [°]	165	(4)
$\log(L_{\rm IR}/{\rm L}_\odot)$	10.04	(5)
SFR ($\mathrm{M}_\odot\,\mathrm{yr}^{-1}$)	1.6	(6)

(1) NASA Extragalactic Database (NED), (2) Wang and Rowan-Robinson (2009), (3) Calculated using INCLINET (Kourkchi et al. 2020), (4) Moustakas et al. (2023), (5) 8–1000 μm IR luminosity calculated from the IRAS flux following Sanders and Mirabel (1996), (6) Estimated from the IR luminosity following Heesen et al. (2018).

2 Observations and data reduction

The observations of NGC 5729 were conducted using the Jansky Very Large Array (JVLA) at 1.5 GHz (L band) and 3 GHz (S band) between 2022 and 2023 (Projects ID 22B-114 and 23A-020), with total on-source times between 0.54 and 0.72 hours. The L-band data were obtained in C configuration, while the S-band data were

acquired in both the B and C configurations. The flux calibrators were observed at the beginning and end of each session, while the phase calibrator was observed between target scans. The observational parameters are listed in Table 2.

Data flagging and calibration were performed using the Common Astronomy Software Applications package (CASA, CASA Team et al. 2022). Standard interferometric calibration procedures were applied, including flux, bandpass and gain calibrations. Self-calibration was applied in both amplitude and phase to improve image quality. For further analysis, visualization and multiwavelength imaging, we used the MIRIAD software package (Sault et al. 1995) and the Cube Analysis and Rendering Tool for Astronomy (CARTA, Comrie et al. 2021). Primary beam correction was performed using CASA.

Imaging was carried out using the CLEAN algorithm with wide-field techniques. Brigg's robust weighting was applied using a *uv* range of 58 kλ for both bands. In addition, S-band images were produced using only the C configuration to ensure consistent *uv* coverage with the L-band data when constructing spectral index maps. These images were used exclusively for this purpose, while all other analyses were performed using the combined B+C configuration data. We also generated an S-band image with uniform weighting (same *uv* range) to take advantage of its higher angular resolution; its application to source identification and size constraints is discussed in Sections 3.2 and 4.2, respectively. The parameters of all images are listed in Table 3.

3 Results

3.1 Radio continuum maps

As shown in Figure 1, the radio continuum emission of NGC 5729 is detected across the galactic disk in both the L and S bands, with an irregular morphology and no single dominant central peak. Instead, the emission is distributed among several regions along the disk, with a mild asymmetry between the two sides. The overall radial extent of the radio emission is approximately 5.8 kpc in the L band and 4.8 kpc in the S band, measured to the 3σ level.

Discrete radio sources are also detected across the disk, as identified in the lower-left panel of Figure 1, which shows the S-band continuum emission. The brightest one, NGC 5729-R1, is located on the northern side of the galaxy, within the galactic disk, at a projected distance of 5.8 kpc from the galaxy center. It is the brightest radio feature detected in NGC 5729 in both bands, exceeding the emission from the central region of the galaxy. A zoom-in of this source, combining the uniformly weighted S-band image with the optical DESI Legacy Survey image, is shown in Figure 2. The source remains unresolved at the angular resolution of the observations. Two fainter sources, NGC 5729-R2 and NGC 5729-R3, are detected at projected radial distances relatively close to the galaxy center, but at vertical distances of approximately 1.5 and 1.8 kpc from the galactic plane, respectively. R2 and R3 are located on the eastern and western sides of the disk, respectively.

No compact source is observed at the galactic center, suggesting the absence of an active nucleus.

3.2 Flux densities and discrete sources

We obtained integrated flux densities for NGC 5729 by summing all emission above the 3σ contour level in the images. The resulting total flux densities are 39 ± 2 mJy at L band and 15.3 ± 0.8 mJy at S band, including the contributions from the discrete sources NGC 5729-R1, R2, and R3.

The flux densities of the discrete sources were measured by integrating the emission within elliptical regions centered on each source. The semi-major and semi-minor axes of these regions were set to the corresponding FWHM values of the synthesized beam, such that the full axes of the integration regions are twice the beam FWHM. A 5% absolute flux calibration uncertainty was adopted in all cases. The flux densities reported in Table 4 were measured from the Briggs-weighted images, which were used consistently across both bands for the spectral index calculations. The source positions were determined from 2D Gaussian fits to the S-band images. For NGC 5729-R1, we also measured its S-band flux density using the uniform-weighted image (which provides higher angular resolution), obtaining 1.53 ± 0.05 mJy, slightly lower than the Briggs-weighted value.

Table 2 JVLA observations parameters. ν and $\Delta\nu$ are the central frequency of the band and its bandwidth, respectively.

Configuration	Band	ν (GHz)	$\Delta\nu$	Date	Time (h)	Antennas	Calibrator sources
C	L	1.5	1.0	2023 Jan. 9	0.72	25	3C 286, J1448-1620
C	S	3.0	2.0	2022 Oct. 25	0.57	26	3C 286, J1448-1620
B	S	3.0	2.0	2023 May 10	0.54	26	3C 286, J1448-1620

Table 3 Image parameters.

Band	Config.	uv range (kλ)	Weighting	B_{maj} (arcsec)	B_{min}	B_{PA} (deg)	rms μJy beam^{-1}
L	C	0-58	Briggs	8.83	5.01	27.06	30
S	C	0-58	Briggs	8.44	5.40	-18.37	15
S	B+C	0-58	Briggs	4.63	3.84	-2.24	9
S	B+C	0-58	Uniform	2.67	2.31	-79.99	30

Nevertheless, we adopt the Briggs-weighted measurements throughout for consistency with the spectral index analysis.

3.3 Spectral index distribution

The spectral index is defined through the dependence of the flux density, S_ν, on the frequency, following the convention $S_\nu \propto \nu^\alpha$. To examine the spatial distribution of the spectral index across NGC 5729, we generated spectral index maps between 1.5 GHz (L band) and 3 GHz (S band). To ensure spatial consistency between the two bands, the total-intensity images were re-gridded and convolved to a common angular resolution of $10''$, corresponding to the resolution of the L-band image. The resulting spectral index and error maps (Figure 3) include only regions with emission exceeding 3σ in both bands.

NGC 5729 shows generally steep spectral indices across the map, consistent with non-thermal synchrotron emission. The spectral index becomes steeper with increasing distance from the galactic plane, from $\alpha \sim -0.9$ in the disk to below -1.8 toward the outer parts of the map. The discrete source NGC 5729-R1 has a flatter spectral index, around -0.8; NGC 5729-R2 is also visible in the map, with $\alpha \sim -1.0$. These values are consistent with the spectral indices derived from the integrated flux densities of the individual sources (Table 4). NGC 5729-R3 is not clearly distinguished in the spectral index map and is located in a region where the spectrum is steeper. A region with flatter spectral index, reaching $\alpha \sim -0.5$, is also visible south of the galaxy, although it lies close to the edge of the map, where the uncertainties are larger. The uncertainties remain below 0.2 across the galactic disk and around NGC 5729-R1, but increase toward the outer parts of the map, reaching values above 0.4 in some areas. The spectral index values in these regions should therefore be interpreted with caution.

3.4 Intensity profiles and scale heights

The vertical intensity profiles provide a measure of the extent of the radio continuum emission above the galactic plane. We derived vertical intensity profiles from the total-intensity radio maps and fitted exponential models of the form $I(z) = I_0 \exp(-|z|/z_0)$, where I_0 is the peak intensity and z_0 is the scale height.

The profiles were constructed using the `BoxModels` task of the NOD3 software (Müller et al. 2017), by averaging the radio emission within strips oriented along the major axis of the galaxy. The fitting procedure accounts for the effective beam, which incorporates the galaxy inclination and other observational and geometrical parameters required by the model. We adopted the corresponding input parameters from those listed in Table 1 and used a single central strip of $60''$, positioned to avoid the source NGC 5729-R1.

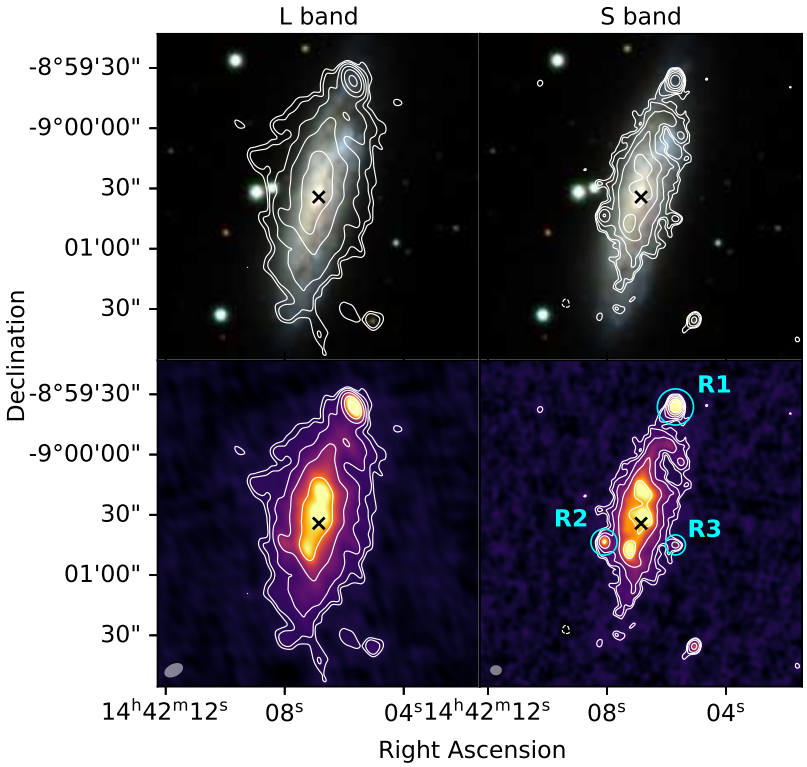


Fig. 1 Radio continuum maps of NGC 5729. L-band (1.5 GHz) and S-band (3 GHz) emission are shown from left to right. The upper panels show the optical DESI Legacy Survey *gri* composite images with overlaid radio contours, while the corresponding total-intensity radio maps are shown in the lower panels. The contour levels are −0.09, 0.09, 0.12, 0.195, 0.383, and 0.851 mJy beam^{-1} for the L band, and −0.027, 0.027, 0.036, 0.0585, 0.115, and 0.255 mJy beam^{-1} for the S band. Negative contours are shown as dashed lines, black crosses mark the galaxy center, and the synthesized beam is shown in the lower-left corner of each radio map. The discrete sources R1, R2, and R3 are highlighted with circular apertures in the lower-right panel.

Table 4 Main properties of discrete sources identified in NGC 5729.

Source	RA_{J2000} hh:mm:ss	DEC_{J2000} dd:mm:ss	$S_{1.5GHz}$ mJy	S_{3GHz} mJy	$L_{1.5GHz}$ 10^{26} erg s^{-1} Hz^{-1}	L_{3GHz} 10^{26} erg s^{-1} Hz^{-1}	α
R1	14:42:05.7	-8:59:36.3	3.0 ± 0.2	1.59 ± 0.08	14.0	7.35	-0.9 ± 0.1
R2	14:42:08.1	-9:00:43.6	0.60 ± 0.05	0.36 ± 0.02	2.80	1.65	-0.8 ± 0.1
R3	14:42:05.7	-9:00:45	0.34 ± 0.04	0.12 ± 0.02	1.56	0.54	-1.5 ± 0.3

Profile points were obtained by averaging pixels within boxes with a horizontal size equal to the strip length and a vertical size of approximately half the synthesized beam (10″ resolution).

We fitted a single-component exponential model to each profile. Two-component models were also tested, but the resulting parameters were poorly constrained, with uncertainties exceeding 100%, indicating that the data do not support the additional model complexity. We therefore adopted the single-component model throughout the analysis. The resulting profiles and best-fit models are shown in Figure 4; fitted parameters are listed in Table 5.

The fitted scale heights are below 1 kpc in both bands (0.84 ± 0.02 kpc at L band and 0.45 ± 0.01 kpc at S band), with uncertainties of about 2%. The L-band scale height is nearly twice the S-band value, although the S-band profile is strongly limited by the angular resolution. These values suggest that the radio emission detected in our observations is largely confined to the galactic

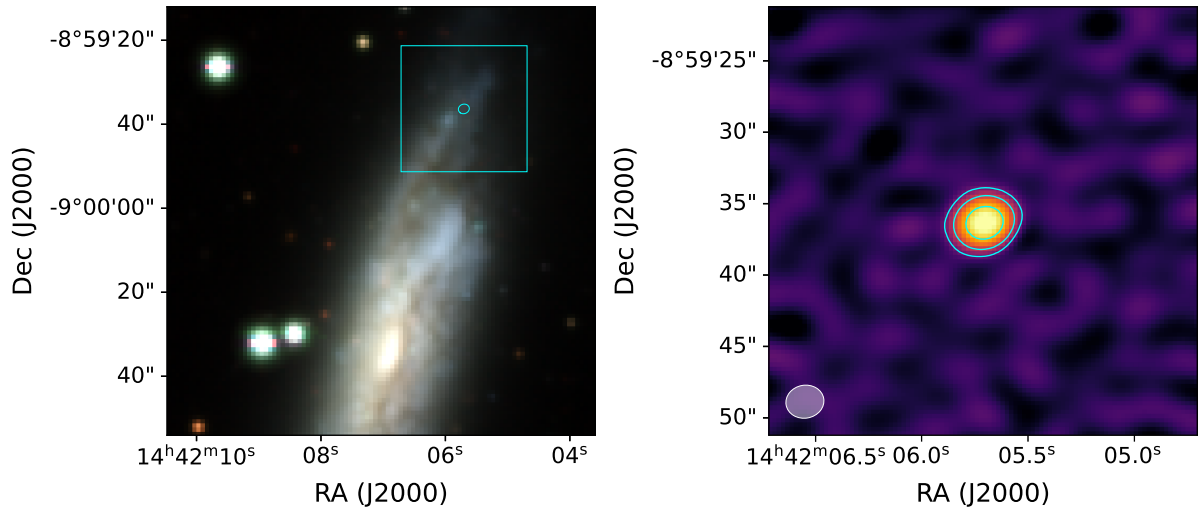


Fig. 2 Zoom-in of the brightest discrete source, NGC 5729-R1. *Left panel*: Optical *gri*-band composite image from the DESI Legacy Survey. The 3σ radio contour from the S-band uniformly-weighted image is overlaid to mark the source position, and the square marks the zoom-in region shown in the right panel, with a side length of $30''$. *Right panel*: S-band uniformly-weighted radio continuum image of the zoom-in region. Contours are drawn at 3, 9, and 27σ, where $\sigma = 30\ \mu\mathrm{Jy\,beam^{-1}}$. The synthesized beam is shown in the bottom-left corner.

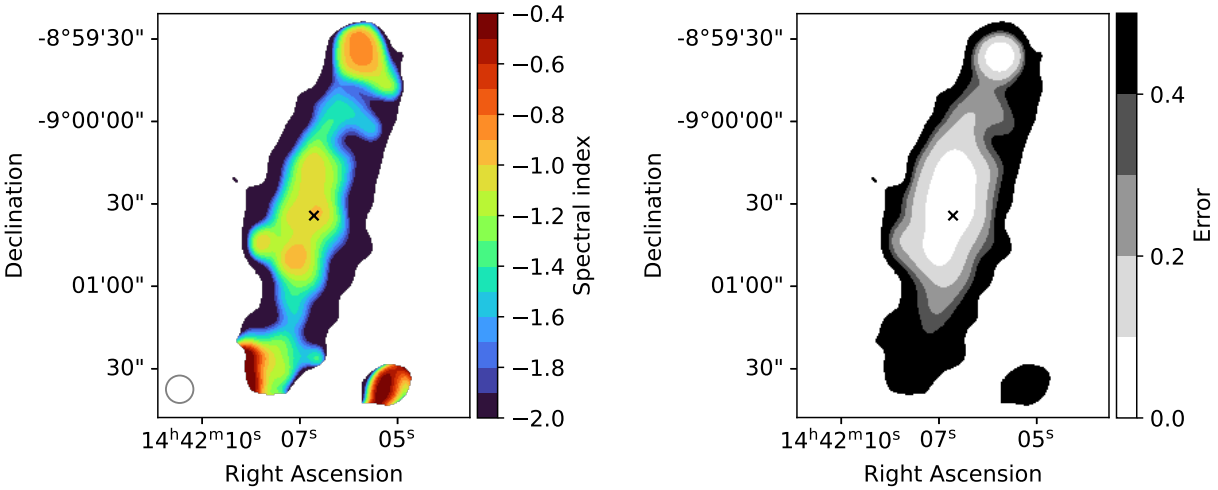


Fig. 3 Spectral index map (left) and corresponding error map (right) for NGC 5729, derived from the 1.5 GHz and 3 GHz images. Spectral indices were computed only for pixels with intensities above three times the noise level in both bands. The beam size is indicated in the bottom-left corner of the left panel.

disk, with no clear evidence for an extended radio halo.

4 Discussion

4.1 Absence of a radio halo

The absence of a prominent radio halo in NGC 5729 is noteworthy given its level of star formation activity. The vertical extent of the radio emission is limited to scale heights of h_S =

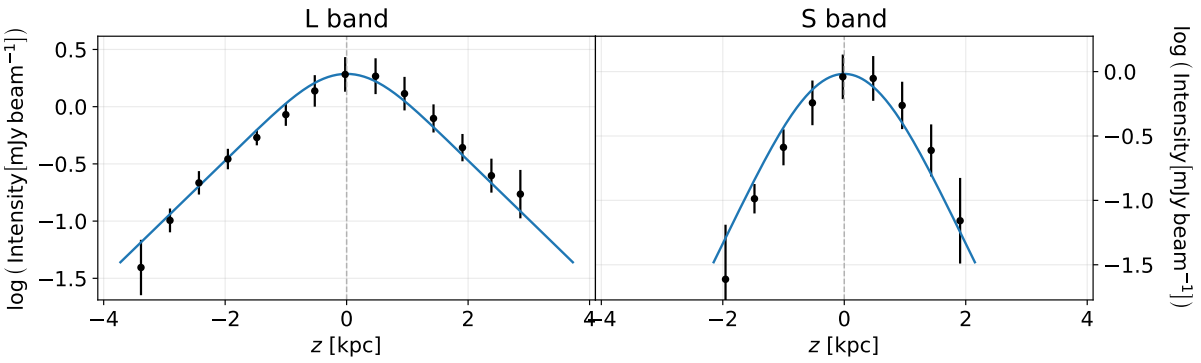


Fig. 4 Average intensity radio continuum profiles and exponential fits of NGC 5729. The left and right panels show the L- and S-band profiles, respectively.

Table 5 Parameters of the best-fitting exponential models to the intensity profiles of NGC 5729.

Band	I_0 mJy beam^{-1}	z_0 kpc
L	2.99 ± 0.06	0.84 ± 0.02
S	2.01 ± 0.04	0.45 ± 0.01

0.45 ± 0.01 kpc and $h_{\rm L} = 0.84 \pm 0.02$ kpc, with no evidence for an additional extended component comparable to the radio halos observed in actively outflowing galaxies. Several factors may contribute to this limited vertical extent (Beck 2015; Krause et al. 2018; Heesen 2021), including the past level and spatial distribution of star formation, the gravitational potential of the galaxy, cosmic-ray energy losses, a very small diffusion coefficient, and the properties of the magnetic field.

Adopting an intermediate star-forming radius of $R = 5.3$ kpc, based on the radial extent of the L- and S-band radio emission, the two independent SFR estimates mentioned in Sect. 1 yield $\Sigma_{\rm SFR}$ values of approximately (10–20) $\times$ 10^{-3} $\mathrm{M_\odot\,yr^{-1}\,kpc^{-2}}$. These values are above the $\Sigma_{\rm SFR} \sim 10^{-3}$ $\mathrm{M_\odot\,yr^{-1}\,kpc^{-2}}$ level associated with the presence of radio halos in the sample of Heesen et al. (2018). This value is better regarded as an empirical lower boundary of the $\Sigma_{\rm SFR}$ values found among galaxies with radio halos, rather than as a sufficient condition for halo formation. In contrast, galaxies such as NGC 4565, UGC 10288, and NGC 4244, which lack prominent extended radio halos, have lower $\Sigma_{\rm SFR}$ values and weak equipartition magnetic fields, with $B_{\rm eq} \lesssim 5, \mu$G (Heesen et al. 2018; Vargas et al. 2019; Xu et al. 2026). However, NGC 5729 exhibits an intermediate level of star-forming activity that approaches the boundary often associated with extraplanar gas excitation. NGC 5729 therefore provides an example of a galaxy with $\Sigma_{\rm SFR}$ above the empirical level associated with radio-halo systems, yet without a prominent extended radio halo. This indicates that the star formation surface density alone does not determine whether an extended radio halo develops.

When placed in the $\log_{10}(h)$ versus $\log_{10}(\mathrm{SFR})$ parameter space of Heesen et al. (2025), the scale height of NGC 5729 falls on the sequence populated by thin radio disks. This is consistent with the small vertical extent measured here and further indicates that a moderate integrated SFR alone is not sufficient to produce an extended radio halo. Instead, efficient radiative cooling combined with in-disk confinement likely depletes the cosmic-ray electron population before they can escape the midplane, preventing the formation of an extended extraplanar synchrotron component.

The gravitational potential may also influence the vertical extent of the radio-emitting plasma. Krause et al. (2018) found an anti-correlation between the normalized radio scale height and the mass surface density in a sample of edge-on spiral galaxies, which they interpreted as evidence for gravitational deceleration of the vertical cosmic-ray transport. NGC 5729 has a stellar mass of $M_\star = 6.5 \times 10^9$ $\mathrm{M_\odot}$, which does not place it among

the most massive spiral galaxies. Thus, while gravitational confinement may contribute to limiting the vertical extent of the radio-emitting plasma, its stellar mass alone does not suggest an exceptionally deep potential well that would readily account for the absence of a radio halo.

An additional constraint is provided by the frequency dependence of the radio scale heights. For NGC 5729, we find $h_{\rm L}/h_{\rm S} = 1.88 \pm 0.07$. For the frequencies considered here, this ratio is substantially higher than the expected values calculated following Krause et al. (2018), which are close to unity for escape-dominated transport (both diffusion and advection) and ~ 1.4 for advection in a halo dominated by synchrotron losses. Although the observed ratio exceeds these idealized expectations, its strong frequency dependence is qualitatively consistent with substantial radiative cooling of the cosmic-ray electrons during vertical transport. In an advective scenario, a relatively low transport velocity would limit the distance traveled by the electrons before they lose a significant fraction of their energy through synchrotron radiation, naturally producing small radio scale heights and preventing the development of an extended synchrotron halo.

The magnetic-field configuration may also affect the efficiency of cosmic-ray transport and the development of an extraplanar synchrotron component. Information on the field strength and geometry, obtained through polarization measurements, would provide an additional constraint on this interpretation, particularly on whether the magnetic field favors vertical transport away from the disk. Such information could help determine whether the limited radio extent is primarily related to cosmic-ray losses, inefficient vertical transport, or a combination of both.

Overall, the relatively high $\Sigma_{\rm SFR}$ of NGC 5729 compared with galaxies lacking prominent radio halos indicates that star formation activity alone does not determine whether an extended radio halo develops. The small radio scale heights and their strong frequency dependence instead point toward substantial cosmic-ray energy losses during transport. A scenario in which cosmic-ray electrons are advected away from the disk at relatively low velocities while undergoing synchrotron cooling provides a possible explanation for the limited vertical extent of the synchrotron emission.

4.2 Discrete sources in NGC 5729

We investigate the nature of the discrete radio sources identified in NGC 5729, focusing on the brightest source detected (NGC 5729-R1). The main observational properties are summarized in Table 4.

The source NGC 5729-R1 is located on the galactic disk, at a projected distance of 5.8 kpc from the galaxy center, spatially coincident with a spiral arm but not associated with a prominent optical HII region. The angular resolution of our radio images corresponds to linear scales of 840×480 pc in L band, 440×370 pc in S band for the Briggs-weighted maps, and 255×220 pc in the uniformly weighted S-band image. Given these resolutions, the source remains unresolved in all images. Therefore, we adopt $\sim 200 - 250$ pc as an upper limit to its intrinsic size, based on the highest-resolution image. The measured flux densities are 3.0 and 1.6 mJy at 1.5 and 3 GHz, respectively, corresponding to spectral luminosities of 1.4×10^{27} and 7.4×10^{26} erg s^{-1} Hz^{-1}, and a spectral index of $\alpha = -0.9 \pm 0.1$, indicative of non-thermal synchrotron emission.

The source could be explained as a collection of supernova remnants (SNRs) or a superbubble powered by multiple supernova explosions. The steep spectral index is consistent with synchrotron emission from SNRs. However, its radio luminosity is significantly higher than that of typical individual remnants. For comparison, Cas A, one of the most luminous Galactic SNRs, would have a flux density of only 0.03 mJy at 3 GHz if placed at the distance of NGC 5729. The observed luminosity of NGC 5729-R1 would therefore require the combined emission of several tens of Cas A-like remnants within a region smaller than 250 pc. This implies an unusually high surface density of SNRs, exceeding even that observed in the central region of M82, where 20–40 SNRs are found within a 600 pc region (Muxlow et al. 1994; Wills et al. 1997). Given that NGC 5729 has a lower global star formation rate and that the source is located outside the nuclear region, such an extreme concentration of SNRs appears unlikely. In addition, the spectral luminosity of NGC 5729-R1 is significantly higher than the typical values found for compact radio sources in nearby edge-on galaxies (Irwin et al. 2022), further disfavoring this scenario.

A purely thermal origin associated with an HII region is strongly disfavored by the observed spectral index. Thermal free-free emission is expected to produce flat spectra ($\alpha \approx -0.1$), in contrast with the steep value measured here. Moreover, the radio luminosity of the source exceeds by several orders of magnitude the brightest known HII regions in the Milky Way and nearby galaxies (Mascoop et al. 2021). This is consistent with previous studies showing that compact radio sources in nearby galaxies are generally not dominated by thermal emission (Irwin et al. 2022). Although a mixed thermal and non-thermal origin cannot be entirely excluded, the emission is clearly dominated by synchrotron radiation.

The possibility that NGC 5729-R1 is a background radio source unrelated to the galaxy must also be considered. Using source counts from simulations of the extragalactic radio sky (Wilman et al. 2008), we estimate the expected number of background sources above a flux density of 3 mJy within the optical extent of NGC 5729. For typical 1.4 GHz source counts ($\sim$ 20–30 sources deg^{-2} at this flux level) we expect $\lesssim 0.02$ background sources. Therefore, while a background origin cannot be excluded, it is statistically unlikely. Nevertheless, examples of such alignments are known in edge-on galaxies (e.g. Irwin et al. 2013; Dumke et al. 2000). In contrast, the source NGC 5729-R1 appears unresolved at our angular resolution and does not exhibit a clear double-lobed morphology, preventing a definitive classification based on radio structure alone.

The properties of NGC 5729-R1 can be compared to those of the well-known microquasar-powered nebula S26, which was initially classified as a supernova remnant and later identified as a ULX-powered system (Pannuti et al. 2002; Pakull et al. 2010; Abaroa et al. 2024). Both sources exhibit steep non-thermal spectral indices and similar upper limits on their physical sizes when placed at comparable distances. Using the flux densities reported by Pannuti et al. (2002), we derive spectral luminosities for S26 that are approximately an order of magnitude lower than those of NGC 5729-R1. If interpreted as a microquasar, this would imply a more powerful jet-driven system than S26. The lack of an X-ray counterpart does not rule out this scenario. Scaling the X-ray luminosity reported for S26 by Pannuti et al. (2002) to the distance of NGC 5729 results in fluxes below the sensitivity limits of the eROSITA survey (Merloni et al. 2024; Tubín-Arenas et al. 2024). Therefore, a microquasar nature cannot be excluded based on currently available X-ray data, and deeper, higher-resolution observations would be required to confirm the presence of a compact accreting source.

In summary, the nature of NGC 5729-R1 remains ambiguous. Its properties are consistent with either a powerful microquasar-driven nebula or an unusually luminous superbubble, although the latter would require extreme conditions. Future high-resolution radio and X-ray observations are essential to distinguish between these scenarios.

The fainter source NGC 5729-R2 exhibits similar spectral properties to NGC 5729-R1, with a steep non-thermal spectral index ($\alpha \approx -0.8$), but lower flux densities and luminosities by approximately an order of magnitude. Given its unresolved nature at our angular resolution and its location within the disk, this source is consistent with a single supernova remnant or a small complex of remnants, although a background origin cannot be excluded.

5 Summary and conclusions

We have presented multi-frequency radio continuum observations of the edge-on spiral galaxy NGC 5729 obtained with the JVLA at 1.5 GHz (L band) and 3 GHz (S band). These observations allow us to characterize the spatially resolved vertical radio structure and the discrete source population of this system. Our main findings are summarized as follows:

1. The integrated flux densities of NGC 5729 are 39 ± 2 mJy at 1.5 GHz and 15.3 ± 0.8 mJy at 3 GHz. Fits to the vertical intensity profiles yield small radio scale heights of $h_{\rm L} = 0.84 \pm 0.02$ kpc and $h_{\rm S} = 0.45 \pm 0.01$ kpc. Despite exhibiting a star formation rate surface density ($\Sigma_{\rm SFR} \sim$ (10-20) $\times\ 10^{-3}$ M$_\odot$ yr^{-1} kpc^{-2}) above empirical thresholds associated with radio halos, the galaxy lacks an extended extraplanar halo. The scale height ratio ($h_{\rm L}/h_{\rm S} = 1.88 \pm 0.07$) indicates a strong frequency dependence, consistent with advective transport at

relatively low velocities where cosmic-ray electrons undergo severe synchrotron energy losses before escaping the disk plane.

2. We detected a prominent discrete radio source, NGC 5729-R1, located in the northern disk at a projected galactocentric distance of 5.8 kpc. The source R1 is the brightest radio feature in the galaxy, exceeding the flux density of the nuclear region. It remains unresolved at our angular resolution, setting an upper limit on its intrinsic physical size of $\lesssim$ 200-250 pc. The source displays a steep non-thermal spectral index ($\alpha = -0.9 \pm 0.1$) and a 1.5 GHz spectral luminosity of 1.4×10^{27} erg s^{-1} Hz^{-1}.
3. A scenario involving a cluster or superbubble of supernova remnants would require several tens of Cas A-like remnants within $\lesssim$ 250 pc, a concentration that is unlikely given the moderate global SFR and off-nuclear location of the source. Alignment with a background AGN cannot be completely ruled out, but is statistically improbable ($\lesssim$ 0.02 expected sources). Instead, the radio properties of R1 are consistent with a powerful microquasar- or ULX-driven nebula, similar to S26 in NGC 7793 but roughly an order of magnitude more luminous in the radio continuum. The current non-detection in eROSITA X-ray data is consistent with this scenario given the sensitivity limits at the distance of NGC 5729.
4. We also detected two fainter discrete sources, NGC 5729-R2 and R3, located at vertical offsets of 1.5 kpc and 1.8 kpc from the midplane, respectively. NGC 5729-R2 displays a non-thermal spectrum ($\alpha \approx -0.8$), consistent with a single SNR or a compact SNR complex.

In summary, while the diffuse radio continuum emission of NGC 5729 is vertically compact due to efficient cosmic-ray energy losses, the radio luminosity of NGC 5729-R1 indicates a localized site of high energy injection in the disk. Higher angular resolution radio observations together with targeted deep X-ray observations will be necessary to resolve the spatial structure of R1 and determine whether it represents a highly luminous microquasar nebula.

Declarations

Funding

GER was supported by the State Agency for Research of the Spanish Ministry for Science and Innovation under grant PID2025-168247NB-C41/AEI/10.13039/501100011033/ and by CONICET (PIP 0835).

Competing Interests

The authors have no relevant financial or non-financial interests to disclose.

Author Contributions

C.A.G. performed data reduction, scale-height analysis, and cosmic-ray transport modeling. J.S. calculated the spectral index maps and contributed to writing the manuscript. P.B. contributed to the review of data calibration and observational procedures. G.E.R. contributed to physical interpretation. All authors revised, reviewed, and approved the final manuscript.

Data Availability

The raw JVLA data are publicly available in the NRAO Science Data Archive under projects ID 22B-114 and 23A-020. Reduced images are available from the corresponding author upon reasonable request.

Ethics Approval

Not applicable.

Acknowledgments

The National Radio Astronomy Observatory is a facility of the National Science Foundation operated under cooperative agreement by Associated Universities, Inc.

References

Abaroa L, Romero GE, Mancuso GC, et al (2024) The remarkable microquasar S26: A super-Eddington PeVatron. A&A691:A93. https://doi.org/10.1051/0004-6361/202450202, arXiv:2409.16315 [astro-ph.HE]

Beck R (2015) Magnetic fields in spiral galaxies. A&ARev24:4. https://doi.org/10.1007/s00159-015-0084-4, arXiv:1509.04522 [astro-ph.GA]

CASA Team, Bean B, Bhatnagar S, et al (2022) CASA, the Common Astronomy Software Applications for Radio Astronomy. PASP134(1041):114501. https://doi.org/10.1088/1538-3873/ac9642, arXiv:2210.02276 [astro-ph.IM]

Cluver ME, Jarrett TH, Dale DA, et al (2025) The S^{4}G-WISE View of Global Star Formation in the Nearby Universe. ApJ979(1):18. https://doi.org/10.3847/1538-4357/ad891b, arXiv:2410.13483 [astro-ph.GA]

Comrie A, Wang KS, Hsu SC, et al (2021) CARTA: The Cube Analysis and Rendering Tool for Astronomy. https://doi.org/10.5281/zenodo.4905459

Condon JJ, Cotton WD, Greisen EW, et al (1998) The NRAO VLA Sky Survey. AJ115(5):1693–1716. https://doi.org/10.1086/300337

Condon JJ, Matthews AM, Broderick JJ (2019) Radio Sources in the Nearby Universe. ApJ872(2):148. https://doi.org/10.3847/1538-4357/ab0301, arXiv:1901.10046 [astro-ph.GA]

Cox DP (2005) The Three-Phase Interstellar Medium Revisited. ARA&A43(1):337–385. https://doi.org/10.1146/annurev.astro.43.072103.150615

Dumke M, Krause M, Wielebinski R (2000) The interstellar medium in the edge-on galaxy NGC 5907. Radio continuum emission and magnetic fields. A&A355:512–524

Ferrière KM (2001) The interstellar environment of our galaxy. Reviews of Modern Physics 73(4):1031–1066. https://doi.org/10.1103/RevModPhys.73.1031, arXiv:astro-ph/0106359 [astro-ph]

Galante CA, Saponara J, Romero GE, et al (2024) Search for radio halos in starburst galaxies. A&A685:A157. https://doi.org/10.1051/0004-6361/202348080, arXiv:2403.05709 [astro-ph.GA]

Giuricin G, Marinoni C, Ceriani L, et al (2000) Nearby Optical Galaxies: Selection of the Sample and Identification of Groups. ApJ543(1):178–194. https://doi.org/10.1086/317070, arXiv:astro-ph/0001140 [astro-ph]

Heald GH, Heesen V, Sridhar SS, et al (2022) CHANG-ES XXIII: influence of a galactic wind in NGC 5775. MNRAS509(1):658–684. https://doi.org/10.1093/mnras/stab2804, arXiv:2109.12267 [astro-ph.GA]

Heesen V (2021) The radio continuum perspective on cosmic-ray transport in external galaxies. Ap&SS366(12):117. https://doi.org/10.1007/s10509-021-04026-1, arXiv:2111.15439 [astro-ph.GA]

Heesen V, Krause M, Beck R, et al (2018) Radio haloes in nearby galaxies modelled with 1D cosmic ray transport using SPINNAKER. MNRAS476(1):158–183. https://doi.org/10.1093/mnras/sty105, arXiv:1801.05211 [astro-ph.GA]

Heesen V, de Gasperin F, Schulz S, et al (2023) Diffusion of cosmic-ray electrons in M 51 observed with LOFAR at 54 MHz. A&A672:A21. https://doi.org/10.1051/0004-6361/202245223, arXiv:2212.06585 [astro-ph.HE]

Heesen V, Stein M, Pourjafari N, et al (2025) CHANG-ES: XXXVI. The thin and thick radio discs. A&A699:A243. https://doi.org/10.1051/0004-6361/202554046, arXiv:2505.13713 [astro-ph.GA]

Irwin J, Krause M, English J, et al (2013) CHANG-ES. III. UGC 10288—An Edge-on Galaxy with a Background Double-lobed Radio Source. AJ146(6):164. https://doi.org/10.1088/0004-6256/146/6/164, arXiv:1311.3894 [astro-ph.GA]

Irwin J, Dyer J, Drake L, et al (2022) CHANG-ES - XXVII. A radio/X-ray catalogue of compact sources in and around edge-on galaxies. MNRAS512(4):5755–5770. https://doi.org/10.

1093/mnras/stac659, arXiv:2202.13225 [astro-ph.GA]

Kourkchi E, Tully RB, Eftekharzadeh S, et al (2020) Cosmicflows-4: The Catalog of ∼10,000 Tully-Fisher Distances. ApJ902(2):145. https://doi.org/10.3847/1538-4357/abb66b, arXiv:2009.00733 [astro-ph.GA]

Krause M, Irwin J, Wiegert T, et al (2018) CHANG-ES. IX. Radio scale heights and scale lengths of a consistent sample of 13 spiral galaxies seen edge-on and their correlations. A&A611:A72. https://doi.org/10.1051/0004-6361/201731991, arXiv:1712.03780 [astro-ph.GA]

Li JT, Beck R, Dettmar RJ, et al (2016) CHANG-ES - VI. Probing Supernova energy deposition in spiral galaxies through multi-wavelength relationships. MNRAS456(2):1723–1738. https://doi.org/10.1093/mnras/stv2757, arXiv:1511.06673 [astro-ph.GA]

Mascoop JL, Anderson LD, Wenger TV, et al (2021) The Galactic H II Region Luminosity Function at Radio and Infrared Wavelengths. ApJ910(2):159. https://doi.org/10.3847/1538-4357/abe532, arXiv:2102.09033 [astro-ph.GA]

Merloni A, Lamer G, Liu T, et al (2024) The SRG/eROSITA all-sky survey. First X-ray catalogues and data release of the western Galactic hemisphere. A&A682:A34. https://doi.org/10.1051/0004-6361/202347165, arXiv:2401.17274 [astro-ph.HE]

Mora-Partiarroyo SC, Krause M, Basu A, et al (2019) CHANG-ES. XIV. Cosmic-ray propagation and magnetic field strengths in the radio halo of NGC 4631. A&A632:A10. https://doi.org/10.1051/0004-6361/201834571, arXiv:1910.07588 [astro-ph.GA]

Moustakas J, Lang D, Dey A, et al (2023) Siena Galaxy Atlas 2020. ApJS269(1):3. https://doi.org/10.3847/1538-4365/acfaa2, arXiv:2307.04888 [astro-ph.GA]

Müller P, Krause M, Beck R, et al (2017) The NOD3 software package: A graphical user interface-supported reduction package for single-dish radio continuum and polarisation observations. A&A606:A41. https://doi.org/10.1051/0004-6361/201731257, arXiv:1707.05573 [astro-ph.IM]

Muxlow TWB, Pedlar A, Wilkinson PN, et al (1994) The structure of young supernova remnants in M82. MNRAS266:455–467. https://doi.org/10.1093/mnras/266.2.455

Pakull MW, Soria R, Motch C (2010) A 300-parsec-long jet-inflated bubble around a powerful microquasar in the galaxy NGC 7793. Nature466(7303):209–212. https://doi.org/10.1038/nature09168

Pannuti TG, Duric N, Lacey CK, et al (2002) An X-Ray, Optical, and Radio Search for Supernova Remnants in the Nearby Sculptor Group Sd Galaxy NGC 7793. ApJ565(2):966–981. https://doi.org/10.1086/337918, arXiv:astro-ph/0112128 [astro-ph]

Sanders DB, Mirabel IF (1996) Luminous Infrared Galaxies. ARA&A34:749. https://doi.org/10.1146/annurev.astro.34.1.749

Sault RJ, Teuben PJ, Wright MCH (1995) A Retrospective View of MIRIAD. In: Shaw RA, Payne HE, Hayes JJE (eds) Astronomical Data Analysis Software and Systems IV, p 433, https://doi.org/10.48550/arXiv.astro-ph/0612759, arXiv:astro-ph/0612759

Schmidt P, Krause M, Heesen V, et al (2019) CHANG-ES. XVI. An in-depth view of the cosmic-ray transport in the edge-on spiral galaxies NGC 891 and NGC 4565. A&A632:A12. https://doi.org/10.1051/0004-6361/201834995, arXiv:1907.03789 [astro-ph.GA]

Tubín-Arenas D, Krumpe M, Lamer G, et al (2024) The eROSITA upper limits. Description and access to the data. A&A682:A35. https://doi.org/10.1051/0004-6361/202346773, arXiv:2401.17305 [astro-ph.HE]

Tumlinson J, Peeples MS, Werk JK (2017) The Circumgalactic Medium. ARA&A55(1):389–432. https://doi.org/

10.1146/annurev-astro-091916-055240, arXiv:1709.09180 [astro-ph.GA]

Vargas CJ, Walterbos RAM, Rand RJ, et al (2019) CHANG-ES. XVII. Hα Imaging of Nearby Edge-on Galaxies, New SFRs, and an Extreme Star Formation Region—Data Release 2. ApJ881(1):26. https://doi.org/10.3847/1538-4357/ab27cb, arXiv:1906.07763 [astro-ph.GA]

Wang L, Rowan-Robinson M (2009) The Imperial IRAS-FSC Redshift Catalogue. MNRAS398(1):109–118. https://doi.org/10.1111/j.1365-2966.2009.15138.x, arXiv:0809.2016 [astro-ph]

Wiegert T, Irwin J, Miskolczi A, et al (2015) CHANG-ES. IV. Radio Continuum Emission of 35 Edge-on Galaxies Observed with the Karl G. Jansky Very Large Array in D Configuration—Data Release 1. AJ150(3):81. https://doi.org/10.1088/0004-6256/150/3/81, arXiv:1508.05153 [astro-ph.GA]

Wills KA, Pedlar A, Muxlow TWB, et al (1997) Low-frequency observations of supernova remnants in M82. MNRAS291(3):517–526. https://doi.org/10.1093/mnras/291.3.517

Wilman RJ, Miller L, Jarvis MJ, et al (2008) A semi-empirical simulation of the extragalactic radio continuum sky for next generation radio telescopes. MNRAS388(3):1335–1348. https://doi.org/10.1111/j.1365-2966.2008.13486.x, arXiv:0805.3413 [astro-ph]

Xu J, Li JT, Liu G, et al (2026) CHANG-ES. XXXVIII. A Thin Radio Halo Shaped by Slow Cosmic-Ray Transport in the Quiescent Galaxy NGC 4565. ApJ1001(2):164. https://doi.org/10.3847/1538-4357/ae5636, arXiv:2603.22417 [astro-ph.GA]